Applied Mathematical Modelling 149 (2026) 116273

Contents lists available at ScienceDirect

Applied Mathematical Modelling

journal homepage: www.elsevier.com/locate/apm

Enhanced wave attenuation through inertial amplification in periodic beam-rigid body structure

N. Rosić [a],*, M. Cajić [b], D. Karličić [b], S. Adhikari [c], M. Lazarević [a]

[a] Department of Mechanics, Faculty of Mechanical Engineering, Kraljice Marije 16, Belgrade, 11120, Serbia
[b] Mathematical Institute of the Serbian Academy of Sciences and Arts, Kneza Mihaila 36, Belgrade, 11001, Serbia
[c] James Watt School of Engineering, The University of Glasgow, Glasgow, G12 8QQ, UK

ARTICLE INFO

Keywords:
Inertial amplifier
Periodic structure
Frequency band structure
Spectral element method
Transfer matrix method

ABSTRACT

We address the fundamental challenge of achieving low-frequency wave attenuation in periodic structures without increasing system mass - a critical limitation in current design of metastructures. Traditionally, low-frequency attenuation has been achieved through the use of local resonators, which can be tuned to a specific low-frequency range by increasing their mass. To overcome this trade-off, we investigate the influence of two inertial amplifiers with distinct configurations: one with auxiliary masses connected to both beam and main mass and another with auxiliary masses suspended between the main mass and a fixed support. The transfer matrix method, combined with the spectral element method, is employed to analyze how design parameters influence the dispersion properties of each system. Our findings show that purposeful structural design of these inertial amplifiers can lead to as much as 50% broader attenuation bands across both high and low-frequency ranges. We also demonstrate near-coupling phenomena between local resonance and Bragg scattering mechanisms, which result in an ultra-wide low-frequency band gap. This study provides a method for robust wave control in periodic structures made of elastic and rigid segments such as buildings and bridges, particularly for low-frequency, lightweight acoustic and seismic isolation.

1. Introduction

Wave propagation through periodic structures with different oscillating attachments has attracted the attention of researchers as it has a significant potential towards vibration suppression. Periodic structures inherently exhibit the so-called “band gaps” - frequency ranges in which elastic waves experience significant attenuation. This phenomenon, known as Bragg scattering, occurs due to dispersive properties of boundaries between tessellated unit cells. The elastic waves are scattered at these boundaries, and waves within the band gap frequencies are eliminated through destructive interference [1–4]. Unlike this mechanism, when the attachments oscillate at their resonant frequency, as they interact with the main structure a band gap is created in the vicinity of that frequency [5–18]. Furthermore, the interaction between these local resonance and Bragg scattering mechanisms can be exploited for efficient wave control [12–14].

Engineered periodic structures are often classified as “metastructures”, as they have properties which surpass the properties of their constituent substructures [3]. These structures are present in aerospace and civil engineering, as well as other engineering fields

---

* Corresponding author.
E-mail address: nrosic@mas.bg.ac.rs (N. Rosić).

https://doi.org/10.1016/j.apm.2025.116273
Received 27 December 2024; Received in revised form 14 June 2025; Accepted 19 June 2025

(e.g., buildings, bridges, pipelines). Despite significant advances in metastructure design for wave control, achieving low-frequency wave attenuation while maintaining system mass and avoiding complex geometries is an ongoing issue. This is especially relevant in civil and aerospace engineering, where such constraints are a priority.

Traditionally, different resonators, such as simple spring-mass resonators (SMRs), have been used to achieve low-frequency band gaps by increasing their mass [5–9]. Local resonance in periodic structures containing elastic beams has been extensively researched for vibration suppression [1], [2], [10–18]. Although these band gaps are often very narrow, in comparison to the band gaps which occur as a result of Bragg scattering, the frequency at which they occur is independent of structural periodicity, and can be tuned more easily as it does not have to satisfy various limits which are imposed on the structural design [13]. The idea of elastic flexural wave filtering using the local resonance band gaps has an application in low-frequency noise and vibration insulation related to the field of aerospace, acoustics, mechanical or seismic engineering [19] and vibrational energy harvesting [20–22]. Due to out of phase response of the attached resonators, negative effective mass or negative effective elastic constants can be perceived near the resonant frequencies [23], [24]. Also, the occurrence of the subwavelength bandgap is a very useful property of local resonance band gaps [23].

In this paper, we explore different methods to induce inertia amplification to passively enhance elastic wave attenuation in periodic structures containing elastic beams and rigid body segments. Our objective is to employ different types of inertial amplifiers to widen existing band gaps and possibly shift them to lower frequencies. The results obtained with inertial amplification mechanisms are compared to those achieved with SMRs of the same static mass. By implementing two different inertial amplifiers with tailored properties [25–30], we explicitly demonstrate the widening and shifting of the attenuation bands toward the low-frequency region without increasing the static mass of the attached discrete systems. This allows for the convenient shifting and expansion of band gaps across all frequency ranges, enabling a range of applications, including wave filtering and the protection of precision instruments from high-frequency noise. Also, interaction can be achieved between the band gaps which occur due to two different mechanisms (Bragg scattering and local resonance), which results in very interesting and useful phenomena, such as near-coupling of these band gaps [11]. It has already been shown that when the frequency ranges of LRBG and BSBG are in close proximity, the width of both band gaps is enhanced [14].

The unit cell under consideration is modeled as two identical elastic beams which have a rigid body suspended between them. The beams are modeled according to Timoshenko beam theory, which includes shear deformations and rotary inertia [2], [31–33]. The rigid body is modeled following a procedure described in [34–36], and its transfer matrix has been derived in accordance with [37]. Implementing the transfer matrix method allows for an efficient manipulation of various equations describing the motion of elastic beams and rigid bodies, giving great advantage during the analysis of investigated periodic mechanical systems [3], [38], [39]. It can also be successfully applied to randomly perturbed and quasiperiodic metastructures [40], [41], as well as periodic structures in which continuity conditions between unit cells do not apply [42]. In combination with the Floquet-Bloch theorem, dispersion properties of the system can be obtained by analyzing a single unit cell [1], [3], [39]. However, the transfer matrix method is suitable only for one-dimensional and quasi-one-dimensional systems, and in the case of large arrays of unit cells it suffers from numerical instability due to unavoidable matrix multiplication [37]. Thus, the spectral element method can be applied by assembling a global dynamic stiffness matrix from the transfer matrix of one unit cell, allowing robust modeling of large systems.

The spectral methods use high-order polynomials which improve convergence properties and the spectral element method combines that with the finite element method [11], [43]. This is particularly advantageous for analytical approach to wave propagation problems in elastic structures, where fewer elements can be used, as structural elements such as beams can be described using beam theories. The advantages of using the spectral element method are twofold: it significantly reduces computational cost compared to the finite element method, and it offers improved precision and numerical stability over the transfer matrix method by avoiding repeated matrix multiplications [32], [33], [44–48]. In this manner, the frequency response function (FRF) for a relatively large number of arrayed unit cells can also be efficiently determined. The FRF which is obtained is plotted against the band diagrams to illustrate the difference between the band gaps resulting from Bragg scattering and the ones which occur due to local resonance [2], [15–18], [38], [44], [49], [50].

This paper introduces a novel metastructure design that integrates suspended inerter-based resonators into periodic beam–rigid body systems to enhance wave attenuation. Unlike prior approaches relying on conventional spring-mass resonators, the proposed method enables significant widening and downward shifting of band gaps without increasing the static mass of the attachments or introducing complex geometrical changes [5–18]. Both inertial amplifiers which are studied in this paper consist of a main mass connected to a beam via a spring, along with two auxiliary masses connected to the main mass using rigid bars. In the first inertial amplifier, the auxiliary masses are connected to both beam and main mass, and in the second mechanism the auxiliary masses are suspended between the main mass and a fixed support. The results are compared with a simple spring-mass attachment, its mass being equal to the total mass of the inertial amplifier. The transfer matrices for the attachments (inertial amplifiers and spring-mass resonator) are derived in accordance with the models presented in [16], [26], [27], [30]. Furthermore, we demonstrate how the interaction between Bragg scattering and local resonance band gaps can be exploited to achieve enhanced vibration suppression. The proposed model captures all critical effects of the rigid body within the system, laying the groundwork for future extensions to more general quasi-one-dimensional metastructures where beams and rigid bodies are connected at arbitrary angles, as well as such quasiperiodic structures. The proposed methodology and procedures can be extended to investigate the influence of discrete systems incorporating materials with complex behaviors, such as plasticity and related anisotropic behaviors, as well as hygro-thermoelastic effects on the deformation of solid structures such as buildings, which occur due to humidity and heat [51], [52]. Experimental validation can also offer valuable insights into the robustness of the analytical formulation of the mathematical model. In the existing literature, experimental studies have been performed on structures incorporating inertial amplification mechanisms and experimental measurements were compared to the FRFs obtained through finite element simulations [53–55].

The paper is organized as follows: In §2, a detailed description of the studied metastructure is provided, along with an explanation of the combined transfer matrix and spectral element methods. In §3 transfer matrices are derived for discrete systems which are attached to provide enhanced wave attenuation. In §4 the details of numerical calculations are given and various results are compared and discussed to demonstrate the effectiveness of the studied inertial amplifiers in shifting and broadening band gaps, as well as their potential for versatile design through tunable parameters. In §5 the main takeaway and several conclusions are provided.

2. Problem statement

We investigate a metastructure made from identical coaxial elastic beams with rigid bodies suspended between every pair of beams, and a discrete system attached at their adjoining ends, as shown in Fig. 1. A unit cell is formed from two Timoshenko beams with one rigid body between them, with an attachment included at the left-most end, as shown in Fig. 2. Harmonic wave motion is assumed, and separation of variables is performed. For example, in the transverse direction, the displacement can be expressed as $w(z,t)=\overline{w}(z)T(t)$. The temporal function $T(t)$ appears as a common factor in all terms and is thus canceled from the matrix equation. The transfer matrix method is used to relate the spatial parts of the state variables at unit cell ends, the state vector being:

$$\boldsymbol{\psi}(z)=\begin{Bmatrix}\overline{w}(z)\\ \overline{\varphi}(z)\\ \overline{M}_f(z)\\ \overline{F}_t(z)\end{Bmatrix}, \tag{1}$$

where z is the longitudinal axis of the unit cell, $\overline{w},\overline{\varphi},\overline{M}_f$ and $\overline{F}_t$ are, respectively, the spatial functions of transverse displacement, angle of rotation of the cross section, bending moment and shearing force. The axial displacement and force are excluded, as no coupling is expected to occur between transverse and axial oscillations when the beams are coaxial [37].

The state vectors at the two ends of the beam are related through the beam transfer matrix $\mathbf{T}_{\text{beam}}$ which is provided in Appendix A together with the relevant beam properties [2], [37]. The transfer matrix for the rigid body $\mathbf{T}_{\text{body}}$ relates the state vectors at two ends of the beams which are adjacent to the rigid body, and it is derived in accordance with [37]:

$$\mathbf{T}_{body}=\begin{bmatrix}1 & D & 0 & 0\\ 0 & 1 & 0 & 0\\ -m\omega^2\frac{D}{2} & J_C\omega^2-m\omega^2\frac{D^2}{4} & 1 & D\\ -m\omega^2 & -m\omega^2 D & 0 & 1\end{bmatrix}, \tag{2}$$

where D denotes the characteristic length of the rigid body, as indicated in Fig. 2, J_C is the mass moment of inertia about the axis which is perpendicular to the plane of motion and passes through the center of mass C of the rigid body.

The transfer matrix for the relevant discrete system which is attached to the left side of the unit cell is denoted as **K**. Thus, the total transfer matrix of such unit cell is obtained through simple matrix multiplication:

$$\mathbf{T}=\mathbf{T}_{\text{beam}}\mathbf{T}_{\text{body}}\mathbf{T}_{\text{beam}}\mathbf{K}=\begin{bmatrix}\mathbf{T}_{11} & \mathbf{T}_{12}\\ \mathbf{T}_{21} & \mathbf{T}_{22}\end{bmatrix}, \tag{3}$$

where $\mathbf{T}_{11}$, $\mathbf{T}_{12}$, $\mathbf{T}_{21}$ and $\mathbf{T}_{22}$ are submatrices (of order 2) of the full transfer matrix $\mathbf{T}$ (of order 4), which relate the relevant components of the state vectors at the two ends of the unit cell. The transfer matrix can be manipulated by simple matrix algebra to obtain the dynamic stiffness matrix for one unit cell [44], [45], which relates the forces and moments to displacements at its ends:

$$\begin{Bmatrix}\overline{M}_f(0)\\ \overline{F}_t(0)\\ \overline{M}_f(\Lambda)\\ \overline{F}_t(\Lambda)\end{Bmatrix}=\begin{bmatrix}\mathbf{T}_{12}^{-1}\mathbf{T}_{11} & -\mathbf{T}_{12}^{-1}\\ \mathbf{T}_{21}-\mathbf{T}_{22}\mathbf{T}_{12}^{-1}\mathbf{T}_{11} & \mathbf{T}_{22}\mathbf{T}_{12}^{-1}\end{bmatrix}\begin{Bmatrix}\overline{w}(0)\\ \overline{\varphi}(0)\\ \overline{w}(\Lambda)\\ \overline{\varphi}(\Lambda)\end{Bmatrix}. \tag{4}$$

Unit cells are tessellated to form the periodic structure, which is modeled by enforcing displacement and force continuity conditions at their interfaces. However, the presented analytical procedure is robust and can be extended to accommodate various discontinuities [42]. For the periodic case considered here, the j-th unit cell satisfies the following matrix equation, where the state variables are consistent with the continuity conditions:

$$\begin{Bmatrix}\overline{M}_{f_j}(0)\\ \overline{F}_{t_j}(0)\\ \overline{M}_{f_{j+1}}(0)\\ \overline{F}_{t_{j+1}}(0)\end{Bmatrix}=\begin{bmatrix}\mathbf{T}_{12}^{-1}\mathbf{T}_{11} & -\mathbf{T}_{12}^{-1}\\ \mathbf{T}_{21}-\mathbf{T}_{22}\mathbf{T}_{12}^{-1}\mathbf{T}_{11} & \mathbf{T}_{22}\mathbf{T}_{12}^{-1}\end{bmatrix}\begin{Bmatrix}\overline{w}_j(0)\\ \overline{\varphi}_j(0)\\ \overline{w}_{j+1}(0)\\ \overline{\varphi}_{j+1}(0)\end{Bmatrix}. \tag{5}$$

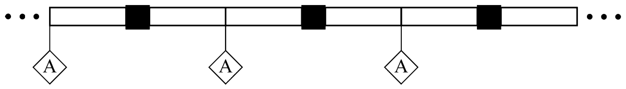

Fig. 1. The system of tessellated unit cells which theoretically extends infinitely in both directions.

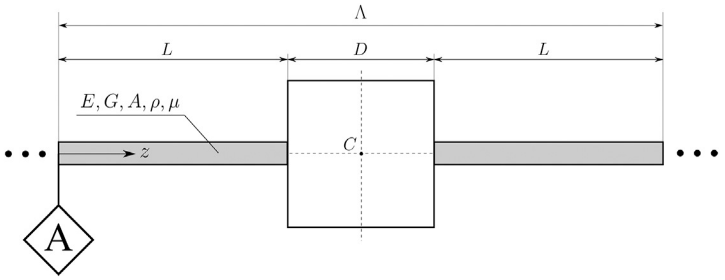

Fig. 2. The unit cell consists of two identical coaxial elastic beams, with a rigid body suspended between them, and an attachment at the left end of the unit cell.

Applying the Floquet–Bloch theorem to two consecutive unit cells, and noting that the internal forces at their boundaries satisfy $\overline{F}_{t_j}(\Lambda) + \overline{F}_{t_{j+1}}(0) = 0$ and $\overline{M}_{t_j}(\Lambda) + \overline{M}_{t_{j+1}}(0) = 0$, we obtain:

$$\left\{\begin{array}{c}\overline{w}_{j+1}(0)\\ \overline{\varphi}_{j+1}(0)\end{array}\right\} = \mathrm{e}^{i\kappa\Lambda}\left\{\begin{array}{c}\overline{w}_{j}(0)\\ \overline{\varphi}_{j}(0)\end{array}\right\}, \left\{\begin{array}{c}\overline{M}_{f_{j+1}}(0)\\ \overline{F}_{t_{j+1}}(0)\end{array}\right\} = -\mathrm{e}^{i\kappa\Lambda}\left\{\begin{array}{c}\overline{M}_{f_{j}}(0)\\ \overline{F}_{t_{j}}(0)\end{array}\right\}, \tag{6}$$

where κ is the wavenumber related to wave propagation through the unit cell as a whole, and $\Lambda = 2L + D$ is the total length of the unit cell, as indicated in Fig. 2. Introducing (6) to (5) leads to:

$$\left(\mathrm{e}^{i2\kappa\Lambda}\mathbf{I} - \mathrm{e}^{i\kappa\Lambda}\mathbf{P}_1 - \mathbf{P}_2\right)\left\{\begin{array}{c}\overline{w}_{j}(0)\\ \overline{\varphi}_{j}(0)\end{array}\right\} = \mathit{0}, \tag{7}$$

which can be transformed to form the eigenvalue problem [44], [45]:

$$\begin{bmatrix}\mathbf{0} & \mathbf{I}\\ \mathbf{P}_2 & \mathbf{P}_1\end{bmatrix}\left\{\begin{array}{c}\overline{w}_{j}(0)\\ \overline{\varphi}_{j}(0)\\ \mathrm{e}^{i\kappa\Lambda}\overline{w}_{j}(0)\\ \mathrm{e}^{i\kappa\Lambda}\overline{\varphi}_{j}(0)\end{array}\right\} - \mathrm{e}^{i\kappa\Lambda}\mathbf{I}\left\{\begin{array}{c}\overline{w}_{j}(0)\\ \overline{\varphi}_{j}(0)\\ \mathrm{e}^{i\kappa\Lambda}\overline{w}_{j}(0)\\ \mathrm{e}^{i\kappa\Lambda}\overline{\varphi}_{j}(0)\end{array}\right\} = \mathit{0}, \tag{8}$$

where

$$\mathbf{P}_1 = \mathbf{T}_{11} + \mathbf{T}_{12}\mathbf{T}_{22}\mathbf{T}_{12}^{-1},$$

$$\mathbf{P}_2 = \mathbf{T}_{12}\mathbf{T}_{21} - \mathbf{T}_{12}\mathbf{T}_{22}\mathbf{T}_{12}^{-1}\mathbf{T}_{11},$$

and **I** is an identity matrix, **0** is a zero matrix of appropriate size, and *0* is a zero vector.

The eigenvalues $e^{i\kappa\Lambda}$ are obtained over a range of frequencies. The dimensionless wavenumber $\kappa\Lambda$ is then calculated and plotted against the dimensionless frequency:

$$\Omega = \frac{\omega\Lambda^2}{2\pi\sqrt{\frac{EI_\xi}{\rho A}}},$$

to produce the band diagram. This diagram illustrates the dispersion properties of the system, helping to visualize the band gaps [32], [33], [46], [47].

In order to validate these results, we plot the frequency response function (FRF) for a system of N unit cells. This is done by building the global dynamic stiffness matrix $\mathbf{M}_N$ and imposing a unit force at the right end of the system, and then solving for displacement vector $V = \mathbf{M}_N^{-1}F$ [44]. The eigenvalue problem and FRF can be obtained using the transfer matrix, as well [32], [33], [38], [46]. However, the large number of matrix multiplications needed for FRF calculation would lead to significant numerical errors. Hence, the spectral element method was used throughout. The first and second to last element of the solution vector V are output and input transverse displacements, w_N and w_1 respectively. The FRF amplitude is then obtained by calculating $20\log_{10}\left(|w_1|/|w_N|\right)$ for each frequency [44].

3. Building the transfer matrix for discrete systems

Here we take into consideration three different discrete systems depicted in Fig. 3, the first being a spring-mass resonator, and the other two different mechanisms intended to cause inertia amplification. Their influence is accounted for by considering the transverse force f_i which is exerted on the beam at their attachment point. Thus, the transfer matrix $\mathbf{K}$ takes the form:

$$\mathbf{K} = \begin{bmatrix} 1 & 0 & 0 & 0 \\ 0 & 1 & 0 & 0 \\ 0 & 0 & 1 & 0 \\ f_i & 0 & 0 & 1 \end{bmatrix}. \tag{9}$$

Understanding the structure of their transfer matrix and the analytical form of the force f_i is essential for comparison, further discussion and analysis of numerical results.

3.1. *The spring-mass resonator*

The spring-mass resonator (SMR) is consisted of a mass m_{res} attached to a spring of stiffness c, as given in Fig. 3.a). The elastic force resulting from the deformation of the spring, due to the transverse displacement of the beam w_i and the displacement of the attached mass v_i, is given by:

$$F_c = c(w_i - v_i). \tag{10}$$

The elastic force acts on the beam at the attachment point, thus $F_c = f_i$. The inertial force $F_{res}^{in} = m_{res}\ddot{v}_i$ is introduced and according to D'Alembert's principle, with respect to directions of forces, we have:

$$F_c - F_{res}^{in} = 0. \tag{11}$$

Consequently, the equation of motion of the attached mass m_{res} is:

$$m_{res}\ddot{v}_i = c(w_i - v_i) = f_i. \tag{12}$$

After applying the harmonic solution for displacements and employing separation of variables, the relevant time derivative is performed, which yields:

$$-m_{res}\omega^2 v_i = c(w_i - v_i). \tag{13}$$

Now, the relationship between displacements v_i and w_i is obtained:

$$v_i = \frac{c}{c - m_{res}\omega^2} w_i, \tag{14}$$

and, according to (12), the force which is exerted by the SMR is:

$$f_i = -\frac{c m_{res}\omega^2}{c - m_{res}\omega^2} w_i. \tag{15}$$

3.2. *The first inertial amplifier*

The first inertial amplifier (IA-1), which is shown in Fig. 3.b), is constituted of a main mass $m_M = 0.5 m_{res}$, which is attached to the beams with a spring of stiffness c. Additionally, two auxiliary masses of mass $m_a = 0.25 m_{res}$ are connected with the beam and the main mass using rigid bars. The angle between the axis of the spring and the rigid bars is θ.

The force-equilibrium diagrams of all masses are illustrated in Fig. 4, where inertial forces $F_w^{in} = m_M \ddot{v}_i$, $F_u^{in} = m_M \ddot{u}_i$ and $F_v^{in} = m_M \ddot{v}_i$ have been introduced. We assume small displacements, thus considering the angle θ to be constant, as well as that the spring remains vertical, thus maintaining the symmetry of the discrete element [26]. Applying the D'Alembert's principle in the direction of displacement v_i results in:

$$2F_2\cos\theta + F_c - F_v^{in} = 0, \tag{16}$$

where $F_c = c(w_i - v_i)$ is the elastic force resulting from the deformation of the spring and $2F_2\cos\theta + F_c = f_i$ is also the force acting on the beam at the attachment point. The equation of motion of the main mass m_M is:

$$m_M\ddot{v}_i = 2F_2\cos\theta + c(w_i - v_i) = f_i. \tag{17}$$

After applying the D'Alembert's principle for an auxiliary mass m_a, in two perpendicular directions of displacements u_i and v_i:

$$F_1\sin\theta + F_2\sin\theta - F_u^{in} = 0, \tag{18}$$

$$F_1\cos\theta - F_2\cos\theta - F_v^{in} = 0, \tag{19}$$

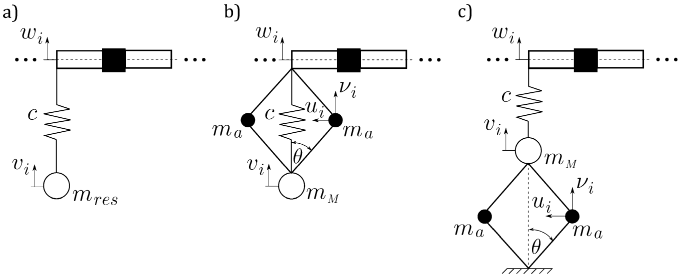

Fig. 3. Unit cells with different attachments: a) spring-mass resonator, b) first inertial amplifier (IA-1), c) second inertial amplifier (IA-2).

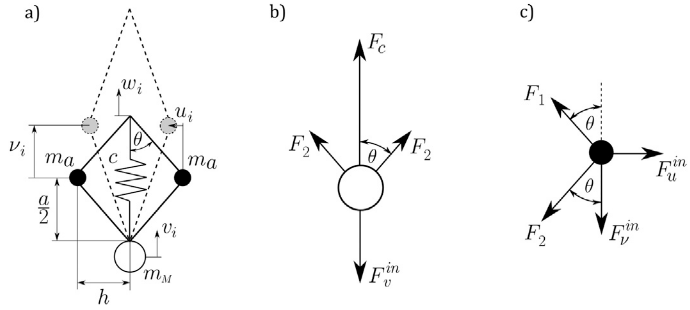

Fig. 4. a) The first inertial amplifier in its undeformed and deformed state (designated with dashed lines), b) the diagram of force equilibrium for the main mass, c) the diagram of force equilibrium for the right auxiliary mass (symmetry applies).

we obtain the equations of motion:

$$m_a \ddot{u}_i = F_1 \sin\theta + F_2 \sin\theta \qquad \Rightarrow -m_a\omega^2 u_i = \left(F_1 + F_2\right)\sin\theta, \tag{20}$$

$$m_a \ddot{v}_i = F_1 \cos\theta - F_2 \cos\theta \qquad \Rightarrow -m_a\omega^2 v_i = \left(F_1 - F_2\right)\cos\theta. \tag{21}$$

The dynamics of both auxiliary masses are identical due to the mechanism's symmetry. To obtain the relationship between u_i and ν_i to v_i and w_i, we follow a procedure analogous to the one which is given in [26], details of which are presented in Appendix B. From Eqs. (20), (21), (B.5) and (B.6) we obtain:

$$F_1 = m_a \frac{\ddot{w}_i - \ddot{v}_i}{4} \frac{1}{\sin^2\theta\cos\theta}, \tag{22}$$

$$F_2 = m_a \frac{\ddot{w}_i - \ddot{v}_i}{4} \frac{\cos 2\theta}{\sin^2\theta\cos\theta}. \tag{23}$$

Finally, from Eqs. (17) and (23) it follows that:

$$-m_M\omega^2 v_i = \left(c - \frac{m_a}{2}\frac{\cos 2\theta}{\sin^2\theta}\omega^2\right)\left(w_i - v_i\right) = k_e\left(w_i - v_i\right) = f_i, \tag{24}$$

where we have introduced the parameter

$$k_e = c - \frac{m_a \cos 2\theta}{2\sin^2\theta}\omega^2 = c - \frac{1}{2}m_a\omega^2\left(\cot^2\theta - 1\right) = c - b\omega^2, \tag{25}$$

where $b = m_a\left(\cot^2\theta - 1\right)/2$. The relation between v_i and w_i is found from (24):

$$v_i = \frac{k_e}{k_e - m_M\omega^2} w_i. \tag{26}$$

Finally, from Eqs. (24) and (26) we obtain:

$$f_i = -\frac{k_e m_M \omega^2}{k_e - m_M\omega^2} w_i, \tag{27}$$

which has the same structure as for SMR, given in Eq. (15), where $k_e = c$ and $m_M = m_{res}$ for SMR. In the case of IA-1, the parameter k_e is also a function of auxiliary mass m_a, the angle θ and angular frequency ω, which indicates that its effects will be more pronounced at higher frequencies.

Analyzing the equation (25) it can be concluded that $\sin\theta = 0$ is not permitted, thus $\theta \neq 0$ (the other solutions are not applicable). In the case when $\theta = \pi/4$, we have $k_e = c$ (as $b = 0$), and the mechanism is reduced to a simple SMR with $m_M = m_{res}/2$.

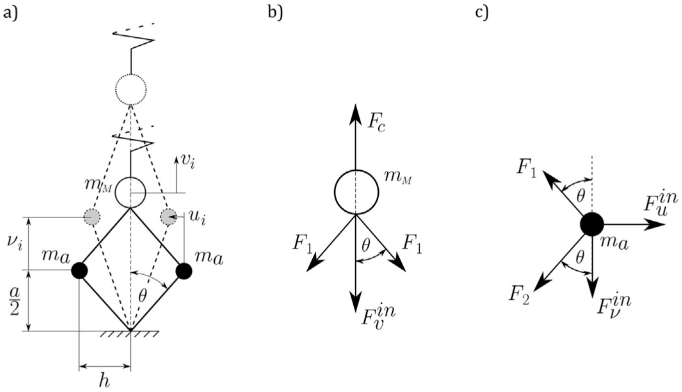

Fig. 5. a) The second inertial amplifier in its undeformed and deformed state (designated with dashed lines), b) the diagram of force equilibrium for the main mass, c) the diagram of force equilibrium for the right auxiliary mass (symmetry applies).

3.3. The second inertial amplifier

When we consider the second inertial amplifier (IA-2), which is presented in Fig. 3.c), we can observe that the main mass is attached to the beam with a spring, while the auxiliary masses are suspended between the main mass and a fixed wall, using the same rigid bars as in IA-1. According to the force-equilibrium diagram presented in Fig. 5.b), and after applying the D'Alembert's principle, the equation of motion for the main mass is obtained:

$$m_M \ddot{v}_i = -2F_1\cos\theta + F_c = -2F_1\cos\theta + c(w_i - v_i) = f_i. \tag{28}$$

The relationship between u_i and ν_i to v_i is provided in Appendix B. Following the similar procedure which was performed for IA-1, and taking into consideration the same equations of motion for auxiliary masses, (20) and (21), we obtain the needed force:

$$F_1 = m_a\frac{\ddot{v}_i}{4}\frac{1}{\sin^2\theta\cos\theta}. \tag{29}$$

Finally, from Eqs. (28) and (29), we find the relation between the motion of the main mass and the transverse motion of the beam at the attachment point:

$$-m_M\omega^2 v_i = c(w_i - v_i) + m_a\frac{v_i}{2\sin^2\theta}\omega^2 \Rightarrow v_i = \frac{c}{k_e' - m_M\omega^2}w_i, \tag{30}$$

where we have introduced the parameter:

$$k_e' = c - \frac{m_a}{2\sin^2\theta}\omega^2 = c - b'\omega^2, \tag{31}$$

where $b' = m_a/2\sin^2\theta$. It can be concluded that in this case $\theta \neq 0$, as well. The unit force is:

$$f_i = -\frac{cm_M\omega^2}{k_e' - m_M\omega^2}w_i, \tag{32}$$

where we can observe that, by comparison to Eqs. (15) and (24), two different parameters, c and k_e', appear in the numerator and denominator, respectively. Unlike the parameter k_e', the spring stiffness c is independent of frequency and the angle θ, which influences the effect of IA-2 on the dispersion properties of the structure.

4. Numerical calculations and results

The unit cell which is used in numerical calculations (Fig. 2) has a square rigid body of side length $D = 0.015$ m and mass $m = 0.005$ kg. The beams are identical, of length $L = 0.05$ m, square cross section with area $A = 1.44 \cdot 10^{-4}\,\mathrm{m}^2$, and shear coefficient $\mu = 5/6$. The beam material is defined by Young's modulus $E = 70$ GPa, shear modulus $G = 27$ GPa and density $\rho = 2713\,\mathrm{kg/m}^3$.

The mass of the spring-mass resonator (Fig. 3.a) is $m_{res} = 0.5\rho AL$, which corresponds to 50% of a single beam's mass. The stiffness of the spring is $c = 0.8EI_\xi/L^3$, representing 80% of beam's bending stiffness, where I_ξ is the second moment of inertia of the cross section of the beam.

The main mass of the first inertial amplifier is set to $m_M = 0.5m_{res}$. Two auxiliary masses, each with $m_a = 0.25m_{res}$, are connected to the beam and the main mass via rigid bars, as shown in Fig. 3.b). Thus, the total mass is equivalent to that of the spring-mass resonator. The main mass is attached to the beam with a spring of stiffness c. The angle between the longitudinal axis of the spring and rigid bars is θ.

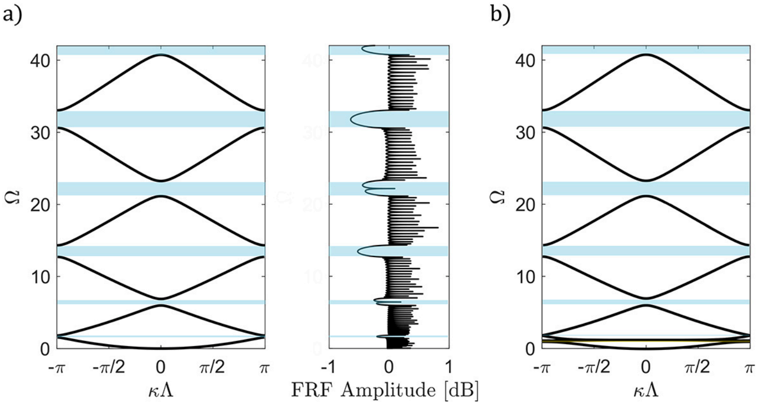

Fig. 6. a) Dispersion diagram and FRF for a unit cell without attachments. The rigid body introduces periodicity to the system, resulting in Bragg scattering band gaps (BSBG), highlighted in blue. b) Dispersion diagram for a unit cell with a spring-mass resonator attached to the left end. The resonator induces a low-frequency local resonance band gap (LRBG) at its resonant frequency.

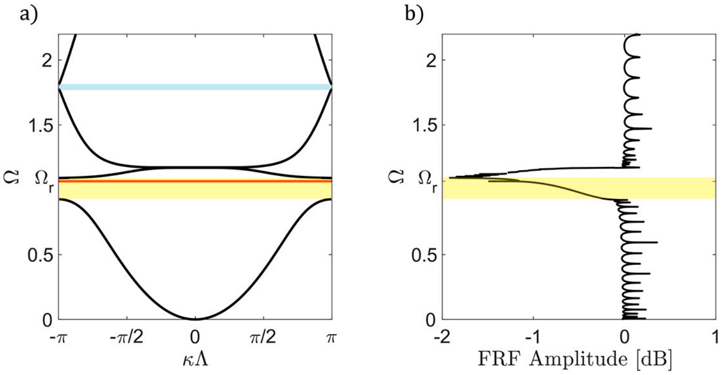

Fig. 7. a) Dispersion diagram and b) frequency response function (FRF) for a system with spring-mass resonators (SMR). A local resonance band gap (LRBG, designated in yellow) is visible at $\Omega_r = 1.06497$ (designated in red). The first BSBG is shifted to a higher frequency and reduced by more than 50% (designated in blue).

The second inertial amplifier contains the same components, except that the auxiliary masses are attached to a fixed wall rather than to the beam, as shown in Fig. 3.c).

The band diagram and frequency response function (FRF) for a system without any attachments is shown in Fig. 6.a). A number of band gaps are observed within the calculated frequency range (highlighted in blue), and FRF indicates that this is due to Bragg scattering band gaps (BSBGs). Since the beams surrounding the rigid body are identical, removing the rigid body would result in no attenuation bands, which is characteristic for a uniform beam [37].

An initial comparison is made with the results for a system with spring-mass resonators (SMR), which are shown in Fig. 6.b). The lower frequency range is shown in Fig. 7, along with the corresponding FRF. A local resonance band gap (LRBG), highlighted in yellow, is observed near the natural frequency of the resonator $\Omega_r = 1.06497$, indicated by a red line. As a consequence, the lowest BSBG which can be seen in Fig. 6.a) shifts to a higher frequency and decreases in size by more than 50%. Beyond the lower frequency range which is shown in Fig. 7, the spring-mass resonator does not affect the dispersion characteristics, which can be observed in Fig. 6, as all band gaps beyond the low-frequency range have not changed.

When the first inertial amplifier (IA-1) is considered, its dispersion characteristics are compared with those of the SMR in Fig. 8. For $\theta = 10°$, there is a significant downward shift of the lower branch in each pair of dispersion branches. Conversely, for $\theta = 70°$, the shift is upward.

Unlike the spring-mass resonator which affects the dispersion characteristics only near its resonant frequency, the first inertial amplifier with the same static mass and spring stiffness induces band gaps of Bragg type across the entire frequency range. The BSBGs caused by IA-1 merge with the ones caused by the rigid body, resulting in much wider band gaps for lower values of θ. A similar effect could be achieved with spring-mass resonators if their stiffness were increased by at least an order of magnitude, as previously discussed in [2]. For higher values of θ, the band gaps between pairs of dispersion branches are slightly wider, but this enlargement is insignificant in comparison to the changes observed for smaller values of θ. The most significant effect of IA-1 at higher θ values occurs in the low-frequency range.

In Fig. 8.a), the broadest BSBG, spanning the frequency range $\Omega \in (28.4933, 33.0388)$, is highlighted in blue. This band gap is nearly twice as large as the corresponding band gap for the SMR case, located at $\Omega \in (30.6321, 33.0412)$. This enlargement occurs at the expense of the BSBG between the pairs of dispersion curves. The BSBG which is highlighted in red for a system with SMR,

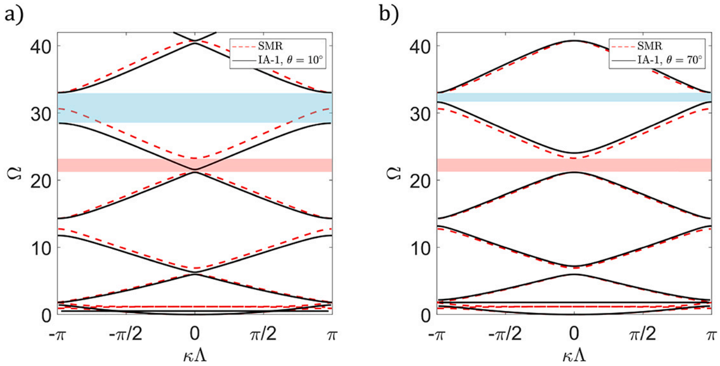

Fig. 8. Comparison of dispersion diagrams for the spring-mass resonator and the first inertial amplifier for: a) $\theta = 10^\circ$ and b) $\theta = 70^\circ$. In the case when $\theta = 10^\circ$, the band gaps between dispersion branches (with the largest highlighted in blue) are widened at the expense of the band gaps between the pairs of dispersion branches, as compared to the BSBG of the SMR system (designated in red). For $\theta = 70^\circ$ the opposite trend is observed.

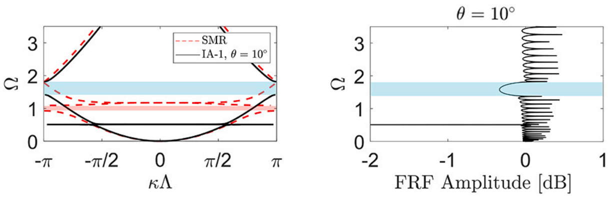

Fig. 9. Comparison of dispersion diagrams for the spring-mass resonator and the first inertial amplifier for $\theta = 10^\circ$ in the low frequency range. The SMR band gap is designated in red (LRBG). The IA-1 band gaps are designated in blue (BSBG) and yellow (LRBG).

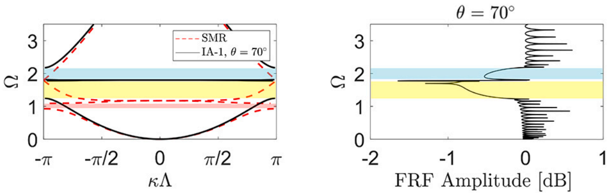

Fig. 10. Comparison of dispersion diagrams for the spring-mass resonator and the first inertial amplifier for $\theta = 70^\circ$ in the low frequency range. The SMR band gap is designated in red (LRBG). The IA-1 band gaps are designated in blue (BSBG) and yellow (LRBG).

and was shown in Fig. 6 to occur due to the presence of the rigid body in the system, is almost completely closed for $\theta = 10^\circ$. By comparing the designated band gaps in Fig. 8, it can be concluded that this effect is reversed for higher values of θ. The limiting value at which this reversal occurs is $\theta = 45^\circ$. According to the factor $\cos 2\theta / \sin^2\theta$ in Eq. (25), when $\cos 2\theta = 0$ (for $\theta = 45^\circ$), there will be no difference in size between the band gaps of Bragg type (in the entire frequency range). Additionally, the LRBG will shift to a lower frequency (because $m_M = 0.5 m_{res}$).

In Fig. 9, where the lower frequency range is shown in detail for $\theta = 10^\circ$, significant differences are observed compared to the system with SMR. A large split in the dispersion branches is evident at $\Omega \in (1.42108, 1.81343)$ (caused by Bragg scattering and highlighted in blue), while the LRBG is narrower and shifted to lower frequencies ($\Omega \approx 0.5$) compared to its position for SMR (Ω_r).

At $\theta = 70^\circ$, which is shown in Fig. 10, the dispersion characteristics are very different, with the BSBG (designated in blue) at a higher frequency $\Omega \in (1.81104, 2.17229)$ and a much wider LRBG at $\Omega \in (1.24643, 1.79907)$, which is designated in yellow. In this case, the LRBG frequency range is higher than the resonant frequency Ω_r of the SMR, but the most significant contribution is the width of the LRBG and the fact that there is a near-coupling between the LRBG and the BRBG, forming a very wide band gap.

This transition is better illustrated in Fig. 11, where dimensionless frequency is plotted against the angle θ. The interplay between Bragg scattering and local resonance effects is visualized as a gradual transformation between the band diagrams for $\theta = 10^\circ$ and $\theta = 70^\circ$. As θ increases, the LRBG widens and shifts to higher frequencies, while the BSBG narrows and is effectively pushed into a higher frequency range, where it grows larger with further increases in θ. For large values of θ, a near-coupling phenomenon is observed between two band gaps which occur as a result of two different mechanisms (Bragg scattering and local resonance) [11]. In this way, a very wide attenuation zone is formed. These results demonstrate that the use of IA-1 provides significant efficiency and versatility in band structure design, particularly for achieving low-frequency attenuation.

For the second inertial amplifier (IA-2), Fig. 12 shows that changes in the dispersion characteristics, compared to the SMR system, occur only at lower frequencies. The higher frequencies remain unaffected because the parameter k_e' (which is a function of θ and angular frequency ω) appears exclusively in the denominator of Eq. (32), which can be expressed as:

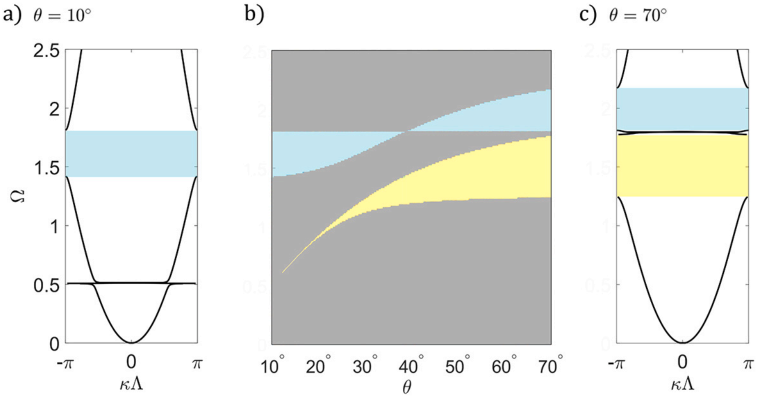

Fig. 11. Band diagram transformation for IA-1, when $\theta \in [10^\circ, 70^\circ]$. The width and frequency level of the LRBG (yellow) increases significantly as θ increases. The width of the BSBG (blue) decreases and it is practically pushed over to a higher frequency range where its width increases again.

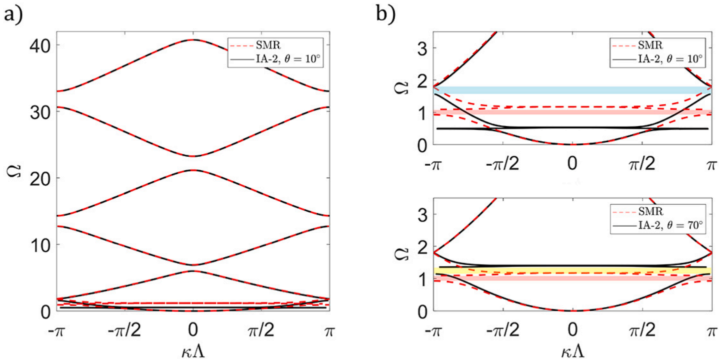

Fig. 12. a) Comparison of the dispersion diagram for SMR and IA-2 for $\theta = 10^\circ$. It can be seen that IA-2 does not influence the dispersion characteristics at higher frequencies. b) Comparison of an enlarged part of a lower frequency range for SMR and IA-2, when $\theta = 10^\circ$ and $\theta = 70^\circ$. The SMR band gap is designated in red (LRBG). The IA-2 band gaps are designated in blue (BSBG) and yellow (LRBG).

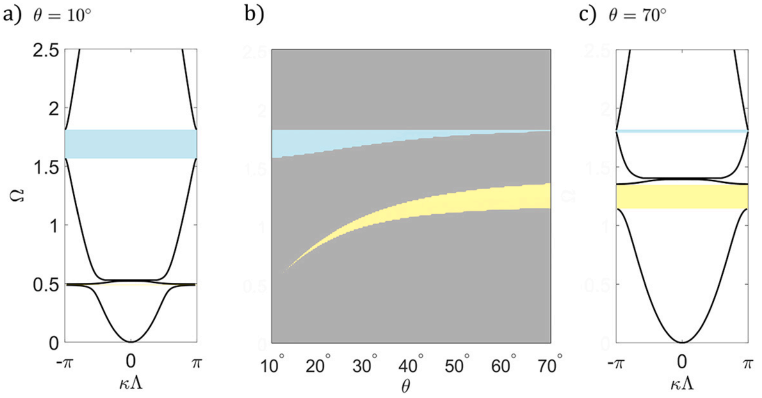

Fig. 13. Band diagram transformation for IA-2, when $\theta \in [10^\circ, 70^\circ]$. The width and frequency level of the LRBG (yellow) increases significantly as θ increases. The effect on the BSBG is opposite.

$$f_i^{\text{IA-2}} = -w_i \frac{c m_M}{\frac{c}{\omega^2} - b' - m_M}.$$

In comparison, for the first inertial amplifier the corresponding expression is:

$$f_i^{\text{IA-1}} = -w_i \frac{(c-b) m_M \omega^2}{\frac{c}{\omega^2} - b - m_M},$$

which is proportional to ω^2. Thus, the influence of IA-2 is lost at higher frequencies and no changes in the BSBGs are observed. Unlike for the case of elastic foundation, which is discussed in [2], this cannot be compensated by increasing the stiffness of the spring.

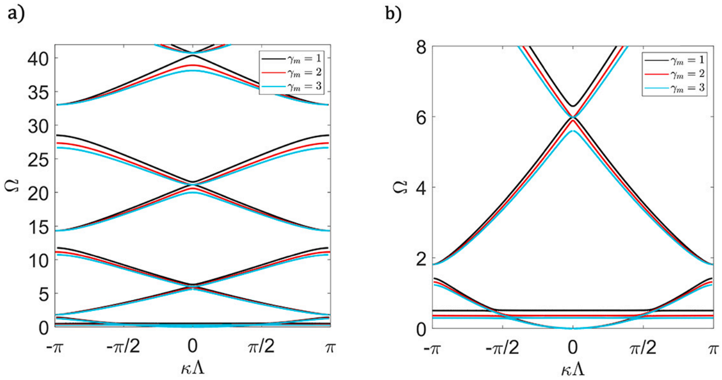

Fig. 14. Mass tuning for IA-1, when $\theta = 10°$: a) the entire calculated frequency range, b) the low-frequency range. The increase of total mass of IA-1 leads to a downwards shift of the LRBG and widens the existing BRBGs between pairs of dispersion branches in each mode.

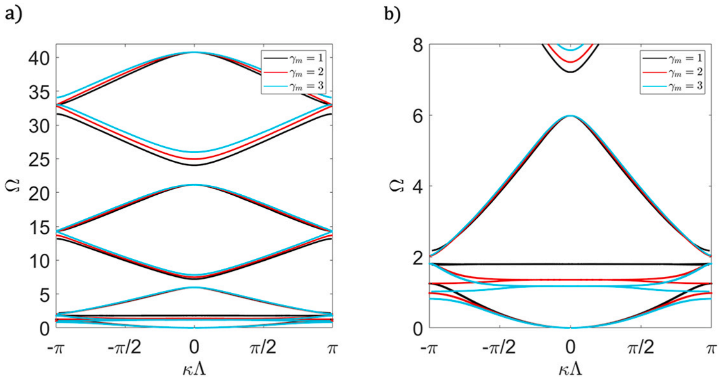

Fig. 15. Mass tuning for IA-1, when $\theta = 70°$: a) the entire calculated frequency range, b) the low-frequency range. The increase of total mass of IA-1 leads to a downwards shift of the LRBG and widens the existing BRBGs between modes.

The results in Fig. 12.b), which presents the lower frequency range in detail, indicate that the LRBG shifts to lower frequencies for smaller angles θ (leading to a wider BSBG), and vice versa. Similar effects would be gained by increasing the mass of SMR. Thus, for small values of θ, a significant reduction in the resonant frequency is achieved without increasing the static mass of the resonator (inertia amplification), although the LRBG becomes more narrow.

In Fig. 13, the dimensionless frequency is plotted against the angle θ. At higher θ values, the influence of the factor $\sin^{-2}\theta$ in b' decreases. Thus, when the LRBG occurs in proximity of the BSBG frequency range, the dominance of local resonance effects is displayed as BSBG becomes more narrow due to wave localization which is caused by the presence of IA-2 [13]. This is also demonstrated in Fig. 12.b), where the difference between band diagrams for SMR and IA-2 (for $\theta = 70°$), is only a small shift of the LRBG to a higher frequency range.

To isolate the influence of the inertial amplifier mass, we scale the total mass to $m_{tot} = \gamma_m \left(m_M + 2m_0\right)$. It is expected for the LRBG to shift to a lower frequency when total mass is increased. As for the BRBGs, it has been shown that the IA-2 has no influence on such band gaps which are not in vicinity of the LRBG, so only the total mass influence of IA-1 will be examined. Thus, the band structure is compared for the cases when total mass is multiplied by the factor γ_m which takes values 1, 2 or 3 (equal, double or triple mass).

In Fig. 14 the results are compared for the case when $\theta = 10°$, and in Fig. 15 for the case when $\theta = 70°$. In Fig. 14.a) and 15.a) the whole calculated frequency range is shown, and in Fig. 14.b) and 15.b) only the lower frequency range is presented. As expected, it can be observed that, regardless of the angle θ, the increase of total mass leads to a downward shift of the LRBG.

However, when BRBGs are considered, for lower values of the angle θ the increase in total mass leads to a significant shift of dispersion branches, which causes wider BRBGs, especially between pairs of dispersion branches within each mode. For higher values of the angle θ, the shift of dispersion branches leads to much larger band gaps between modes.

Upon further examination, in the case when $\theta = 10°$, if only mass m_M is increased by the same factor γ_m (making the total mass $m_{tot} = \gamma_m m_M + 2m_0$), we obtain almost the same diagram as in Fig. 14. When only the auxiliary mass is increased (the total mass being $m_{tot} = m_M + 2\gamma_m m_0$), there is imperceptible difference to the case when $\gamma_m = 1$ (there is almost no change in band gaps for different values of γ_m). In the case when $\theta = 70°$, the effect is opposite. Thus, mass tuning is most effective when applied to m_M at small angles θ and to m_a at large angles θ. These results are omitted for the sake of brevity (as these diagrams look the same as in Fig. 14 and 15).

Since $\cot 45° = 1$, for $\theta > 45°$ we have $(\cot^2\theta - 1) < 0$, which results in $b < 0$. As b changes sign, k_e becomes significantly larger and dominates over the influence of the mass m_M. Conversely, when $\theta < 45°$, the influence of m_M becomes dominant relative to k_e.

In both cases, the LRBG shifts to lower frequencies as the total mass increases. However, only the appropriate mass component has a significant impact on BRBGs.

5. Conclusion

This paper provides valuable insights which can contribute to low-frequency acoustic and seismic engineering through application and tuning of different inertial amplifiers. Two distinct mechanisms (IA-1 and IA-2) were used to achieve significant wave attenuation compared to traditional spring-mass resonators, while maintaining the same total mass. Additionally, the mass tuning capabilities were investigated for IA-1. By combining the transfer matrix and spectral element methods, we developed a robust procedure for analyzing dispersive behavior and demonstrated how both local resonance and Bragg scattering contribute to wider and more tunable band gaps.

We have demonstrated that a purposeful configuration of inertial amplifiers can shift band gaps to desired frequency ranges while maintaining or enhancing their width, offering new possibilities in the design of such metastructures. This approach is particularly effective in the lower frequency range, where traditional solutions struggle. By analyzing the conditions that lead to the near-coupling phenomenon between local resonance and Bragg scattering mechanisms, remarkable control over wave propagation is achieved, providing ultra-wide low-frequency band gaps for higher angles in the IA-1 structure. It was also demonstrated that through mass tuning in IA-1, both low and high frequency ranges can be affected, in contrast to the traditional SMR, which only shifts its resonant frequency. The second configuration, IA-2, was shown to be less effective than IA-1, but remains useful for manipulating low-frequency attenuation zones through local resonance effects.

These findings have significant implications for various engineering applications, particularly in fields requiring lightweight solutions for vibration isolation and wave control. The ability to achieve enhanced low-frequency attenuation without the increase of mass opens new possibilities in seismic protection, aerospace structures, and precision instrument isolation. Future research directions should explore the extension of these concepts to investigate nonlinear effects in the inertial amplification mechanisms, and develop optimization strategies for specific application requirements. Additionally, experimental validation of these theoretical predictions would provide valuable insights for practical implementation, particularly regarding manufacturing tolerances and structural damping effects.

CRediT authorship contribution statement

N. Rosić: Writing – original draft, Software, Methodology, Conceptualization. **M. Cajić:** Writing – review & editing, Supervision. **D. Karličić:** Writing – review & editing, Supervision. **S. Adhikari:** Writing – review & editing, Conceptualization. **M. Lazarević:** Writing – review & editing, Supervision.

Declaration of competing interest

The authors declare the following financial interests/personal relationships which may be considered as potential competing interests: Nevena Rosic reports financial support was provided by Ministry of Science, Technological Development and Innovation of the Republic of Serbia. Milan Cajic reports a relationship with Mathematical Institute of the Serbian Academy of Sciences and Arts that includes: employment. Danilo Karlicic reports a relationship with Mathematical Institute of the Serbian Academy of Sciences and Arts that includes: employment. Sondipon Adhikari reports a relationship with James Watt School of Engineering, The University of Glasgow that includes: employment. Mihailo Lazarevic reports a relationship with University of Belgrade Faculty of Mechanical Engineering that includes: employment. If there are other authors, they declare that they have no known competing financial interests or personal relationships that could have appeared to influence the work reported in this paper.

Acknowledgements

This research has been supported by the research grant of the Serbian Ministry of Science, Technological Development and Innovations, through the Mathematical Institute SANU and grant No. 451-03-137/2025-03/200105 from 4.2.2025. This support is gratefully acknowledged.

Appendix A

We consider a Timoshenko beam (see Fig. A.16) defined by its geometric properties (length L, a square cross-section of area A and second moment of inertia I_ξ) and material properties (Young's modulus E, shear modulus G and mass density ρ). The Timoshenko shear coefficient is μ. We also introduce the radius of gyration $R_g = \sqrt{I_\xi/A}$ and the longitudinal wave speed $c_0 = \sqrt{E/\rho}$.

To build the transfer matrix, we introduce the matrix $\mathbf{U}$, whose non-zero components are given by [2], [37]:

$$U_{11} = \cos k_1\zeta,\ U_{12} = \sin k_1\zeta,\ U_{13} = \cos k_2\zeta,\ U_{14} = \sin k_2\zeta,$$

$$U_{21} = iS_1 \sin k_1\zeta,\ U_{22} = -iS_1 \cos k_1\zeta,$$

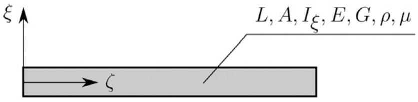

Fig. A.16. Timoshenko beam with its geometric and material properties.

$$U_{23} = iS_2 \sin k_2\zeta,\ U_{24} = iS_2 \cos k_2\zeta,$$
$$U_{31} = -iEI_\xi S_1 k_1 \cos k_1\zeta,\ U_{32} = -iEI_\xi S_1 k_1 \sin k_1\zeta,$$
$$U_{33} = -iEI_\xi S_2 k_2 \cos k_2\zeta,\ U_{34} = -iEI_\xi S_2 k_2 \sin k_2\zeta,$$
$$U_{41} = -\mu GA\left(k_1 + iS_1\right)\sin k_1\zeta,\ U_{42} = \mu GA\left(k_1 + iS_1\right)\cos k_1\zeta,$$
$$U_{43} = -\mu GA\left(k_2 + iS_2\right)\sin k_2\zeta,\ U_{44} = \mu GA\left(k_2 + iS_2\right)\cos k_2\zeta,$$

where:

$$k_1 = \sqrt{\frac{\mu G + E}{2c_0^2\mu G}\omega^2 - \sqrt{\left(\frac{\mu G + E}{2c_0^2\mu G}\right)^2\omega^4 - \frac{\rho\omega^2 R_g^2 - \mu G}{c_0^2 R_g^2\mu G}\omega^2}},$$
$$k_2 = \sqrt{\frac{\mu G + E}{2c_0^2\mu G}\omega^2 + \sqrt{\left(\frac{\mu G + E}{2c_0^2\mu G}\right)^2\omega^4 - \frac{\rho\omega^2 R_g^2 - \mu G}{c_0^2 R_g^2\mu G}\omega^2}},$$
$$S_1 = i\frac{\mu GAk_1^2 - \rho A\omega^2}{\mu GAk_1},$$
$$S_2 = i\frac{\mu GAk_2^2 - \rho A\omega^2}{\mu GAk_2}.$$

The transfer matrix which relates the state vector at the right side of the beam to the state vector at the left side of the beam is:

$$\mathbf{T}_{beam} = \mathbf{U}(\zeta = L)\,\mathbf{U}(\zeta = 0)^{-1}. \tag{A.1}$$

Appendix B

Using the procedure presented in [26], and based on the deformation schemes of considered inertial amplifiers which can be seen in Fig. 4.a and 5.a, we are able to find the relation between the displacement u_i of the auxiliary mass to displacements w_i and v_i. In both mechanisms $\theta \approx const$ due to the small deformations assumption. Thus, bearing in mind that depicted deformation is overly exaggerated, and observing two designated lengths h and $a/2$ (the whole distance from the beam to the main mass being a), we have that $h = (a/2)\tan\theta$. We can also define the displacement u_i as:

$$u_i = h - h', \tag{B.1}$$

where h' designates the same distance in the deformed state. However, it is more convenient to find the difference of squares [26]. If we take the length of one rod to be l, it holds that $l^2 = h^2 + (a/2)^2$. As the rods are rigid, we obtain:

$$h^2 - (h')^2 = \left(l^2 - \frac{a^2}{4}\right) - \left(l^2 - \frac{a'^2}{4}\right) = \frac{a'^2}{4} - \frac{a^2}{4}. \tag{B.2}$$

The difference of squares can be transformed into:

$$h^2 - (h')^2 = \left(h - h + u_i\right)\left(h + h - u_i\right) = u_i\left(2h - u_i\right). \tag{B.3}$$

Relations for the first inertial amplifier In the deformed state, we have $a' = a + w_i - v_i$. It follows that:

$$h^2 - (h')^2 = \frac{1}{4}\left[2a\left(w_i - v_i\right) + \left(w_i - v_i\right)^2\right] = u_i\left(a\tan\theta - u_i\right). \tag{B.4}$$

Due to the assumption of small deformations we can also assume that $\left(w_i - v_i\right)^2 \ll 2a\left(w_i - v_i\right)$ and $u_i \ll a\tan\theta$, thus:

$$u_i = \frac{w_i - v_i}{2\tan\theta}. \tag{B.5}$$

In a similar manner, we can find v_i:

$$v_i = \frac{a'}{2} - \frac{a}{2} = \frac{w_i - v_i}{2}. \tag{B.6}$$

Relations for the second inertial amplifier We have that $a' = a + v_i$, which leads to:

$$h^2 - (h')^2 = \frac{a'^2}{4} - \frac{a^2}{4} = \frac{1}{4}\left(2av_i + v_i^2\right) = u_i\left(2h - u_i\right). \tag{B.7}$$

Since $v_i^2 \ll 2av_i$ and $u_i \ll a\tan\theta$, we have:

$$u_i = \frac{v_i}{2\tan\theta}. \tag{B.8}$$

Finally, for ν_i we have:

$$\nu_i = \frac{a'}{2} - \frac{a}{2} = \frac{v_i}{2}. \tag{B.9}$$

Data availability

Data will be made available on request.

References

[1] D.M. Mead, Wave propagation in continuous periodic structures: research contributions from Southampton, 1964-1995, J. Sound Vib. 190 (1996) 495–524, https://doi.org/10.1006/jsvi.1996.0076.

[2] L. Liu, M.I. Hussein, Wave motion in periodic flexural beams and characterization of the transition between Bragg scattering and local resonance, J. Appl. Mech. 79 (2012) 011003, https://doi.org/10.1115/1.4004592.

[3] M.I. Hussein, M. Ruzzene, M. Leamy, Dynamics of phononic materials and structures: historical origins, recent progress, and future outlook, Appl. Mech. Rev. 66 (2014) 040802, https://doi.org/10.1115/1.4026911.

[4] A. Banerjee, R. Das, E.P. Calius, Waves in structured mediums or metamaterials: a review, Arch. Comput. Methods Eng. 26 (2019) 1029–1058, https://doi.org/10.1007/s11831-018-9268-1.

[5] B. Sharma, C. Sun, Impact load mitigation in sandwich beams using local resonators, J. Sandw. Struct. Mater. 18 (1) (2016) 50–64, https://doi.org/10.1177/1099636215583171.

[6] B. Sharma, C.-T. Sun, Local resonance and Bragg bandgaps in sandwich beams containing periodically inserted resonators, J. Sound Vib. 364 (2016) 133–146, https://doi.org/10.1016/j.jsv.2015.11.019.

[7] J. Zhou, K. Wang, D. Xu, H. Ouyang, Local resonator with high-static-low-dynamic stiffness for lowering band gaps of flexural wave in beams, J. Appl. Phys. 121 (4) (2017) 044902, https://doi.org/10.1063/1.4974299.

[8] T. Wang, M. Sheng, Q. Qin, Multi-flexural band gaps in an Euler-Bernoulli beam with lateral local resonators, Phys. Lett. A 380 (2016) 525–529, https://doi.org/10.1016/j.physleta.2015.12.010.

[9] J.-S. Chen, B. Sharma, C. Sun, Dynamic behaviour of sandwich structure containing spring-mass resonators, Compos. Struct. 93 (8) (2011) 2120–2125, https://doi.org/10.1016/j.compstruct.2011.02.007.

[10] G. Carta, M. Brun, Bloch-Floquet waves in flexural systems with continuous and discrete elements, Mech. Mater. 87 (2015) 11–26, https://doi.org/10.1016/j.mechmat.2015.03.004.

[11] Y. Xiao, J. Wen, G. Wang, X. Wen, Theoretical and experimental study of locally resonant and Bragg band gaps in flexural beams carrying periodic arrays of beam-like resonators, J. Vib. Acoust. 135 (4) (2013) 041006, https://doi.org/10.1115/1.4024214.

[12] M. Cenedese, E. Belloni, F. Braghin, Interaction of Bragg scattering bandgaps and local resonators in mono-coupled periodic structures, J. Appl. Phys. 129 (2021) 124501, https://doi.org/10.1063/5.0038438.

[13] Z. Jia, Y. Chen, H. Yang, L. Wang, Designing phononic crystals with wide and robust band gaps, Phys. Rev. Appl. 9 (2018) 044021, https://doi.org/10.1103/PhysRevApplied.9.044021.

[14] B. Yuan, Y. Chen, M. Jiang, S. Tang, M. He, M. Tu, On the interaction of resonance and Bragg scattering effects for the locally resonant phononic crystal with alternating elastic and fluid matrices, Arch. Acoust. 42 (4) (2017) 725–733, https://doi.org/10.1515/aoa-2017-0075.

[15] D. Yaozong, L. Gang, W. Honggang, Q. Jing, Flexural vibration band gaps in Timoshenko beams with locally resonant structures, J. Appl. Phys. 100 (2006) 124901, https://doi.org/10.1063/1.2400803.

[16] A. Banerjee, Non-dimensional analysis of the elastic beam having periodic linear spring mass resonators, Meccanica 55 (2020) 1181–1191, https://doi.org/10.1007/s11012-020-01151-z.

[17] G. Failla, R. Santoro, A. Burlon, A. Francesco Rusillo, An exact approach to the dynamics of locally-resonant beams, Mech. Res. Commun. 103 (2020) 103460, https://doi.org/10.1016/j.mechrescom.2019.103460.

[18] C. Chesnais, C. Boutin, S. Hans, Effects of the local resonance on the wave propagation in periodic frame structures: generalized Newtonian mechanics, J. Acoust. Soc. Am. 132 (2012) 2873–2886, https://doi.org/10.1121/1.4744975.

[19] H.J. Xiang, Z.F. Shi, S.J. Wang, Y.L. Mo, Periodic materials-based vibration attenuation in layered foundations: experimental validation, Smart Mater. Struct. 21 (11) (2012) 112003, https://doi.org/10.1088/0964-1726/21/11/112003.

[20] G. Hu, L. Tang, R. Das, Internally coupled metamaterial beam for simultaneous vibration suppression and low frequency energy harvesting, J. Appl. Phys. 123 (5) (2018) 055107, https://doi.org/10.1063/1.5011999.

[21] Y. Li, E. Baker, T. Reissman, C. Sun, W.K. Liu, Design of mechanical metamaterials for simultaneous vibration isolation and energy harvesting, Appl. Phys. Lett. 111 (25) (2017) 251903, https://doi.org/10.1063/1.5008674.

[22] K. Devarajan, B. Santhosh, Inertial amplification as a performance enhancement method for snap-through vibration energy harvester, Appl. Math. Model. 137 (2025) 115734, https://doi.org/10.1016/j.apm.2024.115734.

[23] P. Sheng, X.X. Zhang, Z. Liu, C.T. Chan, Locally resonant sonic materials, Physica B, Condens. Matter 338 (1–4) (2003) 201–205, https://doi.org/10.1016/S0921-4526(03)00487-3.

[24] A. Banerjee, R. Das, E.P. Calius, Frequency graded 1D metamaterials: a study on the attenuation bands, J. Appl. Phys. 122 (7) (2017) 075101, https://doi.org/10.1063/1.4998446.

[25] D. Karličić, M. Cajić, S. Paunović, A. Obradović, S. Adhikari, J. Christensen, Non-reciprocal wave propagation in time-modulated elastic lattices with inerters, Appl. Math. Model. 117 (2023) 316–335, https://doi.org/10.1016/j.apm.2022.12.029.

[26] M.M.N. Frandsen, R.O. Bilal, S.J. Jensen, M.I. Hussein, Inertial amplification of continuous structures: large band gaps from small masses, J. Appl. Phys. 119 (2016) 124902, https://doi.org/10.1063/1.4944429.

[27] S. Chowdhury, A. Banerjee, S. Adhikari, A critical review on inertially-amplified passive vibration control devices, Arch. Comput. Methods Eng. 31 (2024) 2139–2175, https://doi.org/10.1007/s11831-023-10040-z.

[28] G. Acar, C. Yilmaz, Experimental and numerical evidence for the existence of wide and deep phononic gaps induced by inertial amplification in two-dimensional solid structures, J. Sound Vib. 332 (24) (2013) 6389–6404, https://doi.org/10.1016/j.jsv.2013.06.022.

[29] Y. Li, N. Zhao, S. Yao, Nonlinear dynamics of 1D meta-structure with inertia amplification, Appl. Math. Model. 118 (2023) 728–744, https://doi.org/10.1016/j.apm.2023.01.039.

[30] P. Celli, A. Palermo, Time modulated inerters as building blocks for nonreciprocal mechanical devices, J. Sound Vib. 572 (2024) 118178, https://doi.org/10.1016/j.jsv.2023.118178.

[31] K.F. Graff, Wave Motion in Elastic Solids, Dover Publications, New York, NY, 1975.

[32] Y.K. Lin, T.J. McDaniel, Dynamics of beam-type periodic structures, J. Eng. Ind. 91 (4) (1969) 1133, https://doi.org/10.1115/1.3591761.

[33] D.J. Mead, A new method of analyzing wave propagation in periodic structures; applications to periodic Timoshenko beams and stiffened plates, J. Sound Vib. 104 (1986) 9–27, https://doi.org/10.1016/S0022-460X(86)80128-6.

[34] A. Obradovic, S. Salinic, D.R. Trifkovic, N. Zoric, Z. Stokic, Free vibration of structures composed of rigid bodies and elastic beam segments, J. Sound Vib. 347 (2015) 126–138, https://doi.org/10.1016/j.jsv.2015.03.001.

[35] A. Tomovic, S. Salinic, A. Obradovic, A. Grbovic, M. Milovancevic, Closed-form solution for the free axial-bending vibration problem of structures composed of rigid bodies and elastic beam segments, Appl. Math. Model. 77 (2020) 1148–1167, https://doi.org/10.1016/j.apm.2019.09.008.

[36] S. Naguleswaran, Vibration of an Euler-Bernoulli stepped beam carrying a non-symmetrical rigid body at the step, J. Sound Vib. 271 (2004) 1121–1132, https://doi.org/10.1016/S0022-460X(03)00574-1.

[37] N. Rosic, D. Karlicic, M. Cajic, S. Adhikari, M. Lazarevic, Wave propagation in tailored metastructures consisting of elastic beams and rigid bodies, Philos. Trans. R. Soc. A 382 (2024) 20230362, https://doi.org/10.1098/rsta.2023.0362.

[38] Z.-C. Wang, W.-J. Yang, K.-V. Yung, A transfer matrix method-based closed-form solution of sensitivities of dynamic properties and FRF for multi-span pipes under complex boundary conditions, Mech. Syst. Signal Process. 198 (2023) 110428, https://doi.org/10.1016/j.ymssp.2023.110428.

[39] M.I. Hussein, G.M. Hulbert, R.A. Scott, Dispersive elastodynamics of 1D banded materials and structures: analysis, J. Sound Vib. 289 (2006) 779–806, https://doi.org/10.1016/j.jsv.2005.02.030.

[40] M. Gupta, M. Ruzzene, Dynamics of quasiperiodic beams, Crystals 10 (2020) 1144, https://doi.org/10.3390/cryst10121144.

[41] G. Carta, M. Brun, A.B. Movchan, T. Boiko, Transmission and localisation in ordered and randomly-perturbed structured flexural systems, Int. J. Eng. Sci. 98 (2016) 126–152, https://doi.org/10.1016/j.ijengsci.2015.09.005.

[42] G. Carta, M. Brun, A.B. Movchan, Dynamic response and localization in strongly damaged waveguides, Proc. R. Soc. A 470 (2014) 20140136, https://doi.org/10.1098/rspa.2014.0136.

[43] T. Jiang, Q. Han, C. Li, Complex band structure and evanescent wave propagation of composite corrugated phononic crystal beams, Acta Mech. 234 (2023) 2783–2808, https://doi.org/10.1007/s00707-023-03522-5.

[44] G. Wang, F. Shi, Z. Chen, Y. Yu, C.W. Lim, Controllable flexural wave bandgap in extensible metamaterial beams with embedded multiple resonators, Contin. Mech. Thermodyn. (2023) 1–19, https://doi.org/10.1007/s00161-023-01228-6.

[45] Z. Chen, G. Wang, F. Shi, C.W. Lim, Analytical modeling and numerical analysis for tunable topological phase transition of flexural waves in active sandwiched phononic beam systems, Int. J. Mech. Sci. 223 (2022) 107292, https://doi.org/10.1016/j.ijmecsci.2022.107292.

[46] G. Carta, M. Brun, Bloch-Floquet waves in flexural systems with continuous and discrete elements, Mech. Mater. 87 (2015) 11–26, https://doi.org/10.1016/j.mechmat.2015.03.004.

[47] M.I.N. Rosa, B.L. Davis, L. Liu, M. Ruzzene, M.I. Hussein, Material vs. structure: topological origins of band-gap truncation resonances in periodic structures, arXiv:2301.00101v1 [cond-mat.mtrl-sci], 2022, https://doi.org/10.48550/arXiv.2301.00101.

[48] N. Fukuwa, S. Matsushima, Wave dispersion and optimal mass modelling for one-dimensional periodic structures, Earthq. Eng. Struct. Dyn. 23 (1994) 1165–1180, https://doi.org/10.1002/eqe.4290231102.

[49] M.S. Kushwaha, P. Halevi, L. Dobrzynski, B. Djafari-Rouhani, Acoustic band structure of periodic elastic composites, Phys. Rev. Lett. 13 (71) (1993) 2022–2025, https://doi.org/10.1103/PhysRevLett.71.2022.

[50] R. Khajehtourian, M.I. Hussein, Dispersion characteristics of a nonlinear elastic metamaterial, AIP Adv. 4 (12) (2014) 124308, https://doi.org/10.1063/1.4905051.

[51] A.K. Yadav, E. Carrera, M. Marin, M.I.A. Othman, Reflection of hygrothermal waves in a nonlocal theory of coupled thermo-elasticity, Mech. Adv. Mat. Struct. 31 (5) (2022) 1083–1096, https://doi.org/10.1080/15376494.2022.2130484.

[52] C. Ghiţă, N. Pop, H. Cioban, Quasi-static behavior as a limit process of a dynamical one for an anisotropic hardening material, Comput. Mater. Sci. 52 (1) (2012) 217–225, https://doi.org/10.1016/j.commatsci.2011.03.030.

[53] G. Acar, C. Yilmaz, Experimental and numerical evidence for the existence of wide and deep phononic gaps induced by inertial amplification in two-dimensional solid structures, J. Sound Vib. 332 (24) (2013) 6389–6404, https://doi.org/10.1016/j.jsv.2013.06.022.

[54] O. Yuksel, C. Yilmaz, Shape optimization of phononic band gap structures incorporating inertial amplification mechanisms, J. Sound Vib. 355 (2015) 232–245, https://doi.org/10.1016/j.jsv.2015.06.016.

[55] A.H. Orta, C. Yilmaz, Inertial amplification induced phononic band gaps generated by a compliant axial to rotary motion conversion mechanism, J. Sound Vib. 439 (2018) 329–343, https://doi.org/10.1016/j.jsv.2018.10.014.